Nuclear Inst. and Methods in Physics Research, A 896 (2018) 139–151

Contents lists available at ScienceDirect

Nuclear Inst. and Methods in Physics Research, A

journal homepage: www.elsevier.com/locate/nima

Emittance measurements in low energy ion storage rings

J.R. Hunt[a,*], C. Carli[b], J. Resta-López[a], C.P. Welsch[a]

[a] *The Cockcroft Institute and The University of Liverpool, United Kingdom*
[b] *European Organization for Nuclear Research, CERN, Switzerland*

ARTICLE INFO

Keywords:
Beam dynamics
Low energy storage rings
Antiprotons
Beam diagnostics
Beam scraping

ABSTRACT

The development of the next generation of ultra-low energy antiproton and ion facilities requires precise information about the beam emittance to guarantee optimum performance. In the Extra-Low ENergy Antiproton storage ring (ELENA) the transverse emittances will be measured by scraping. However, this diagnostic measurement faces several challenges: non-zero dispersion, non-Gaussian beam distributions due to effects of the electron cooler and various systematic errors such as closed orbit offsets and inaccurate rms momentum spread estimation. In addition, diffusion processes, such as intra-beam scattering might lead to emittance overestimates. Here, we present algorithms to efficiently address the emittance reconstruction in presence of the above effects, and present simulation results for the case of ELENA.

1. Introduction

Emittance measurement is essential in all particle accelerators and transfer lines to control and provide the required beam quality. There are many different ways to measure emittance ranging from simple beam optics techniques to new and advanced setups such as the supersonic gas jet based beam profile monitor [1]. In this paper we focus on expanding the capabilities of beam scraping through new data analysis and determine the limits of such a technique using particle tracking simulations.

Beam scraping enables direct access to information on the transverse phase space amplitude. It also presents a high dynamic range very suitable for getting information of low density long tails and halo measurements. Indeed, scraping by collimators has been used to measure beam halo diffusion and population in high energy colliders, e.g. in the Large Electron–Positron collider (LEP) [2] and Tevatron [3] in the past, and more recently in the Large Hadron Collider (LHC) [4].

Despite being destructive, the scraping method has also been used in many hadron machines for emittance measurement. Concretely, due to the simplicity of usage, it has been used with relatively low intensity antiproton beams in the Antiproton Decelerator (AD) [5,6], and a scraper device has been installed to measure emittances in the new ELENA storage ring [7].

As mentioned before, beam scraping is a destructive measurement technique. The beam is completely or partially removed by the scraper. Apart from measuring transverse phase space dimensions of the beam, scrapers can be used as collimators to reduce the size and intensity of the beam if necessary.

There are two types of scraper operation. In some cases the beam is progressively driven into a fixed limiting scraper aperture by means of steering magnets producing a local orbit bump. For instance, this is the functioning principle of the so-called BEAMSCOPE (BEtatron AMplitude Scraping by Closed-Orbit PErturbation) installed in the PS Booster at CERN [8]. However, the most common scraper operation mode is to move the scraper blades into the beam.

In order to directly access the information of the betatron phase space, scraper devices are preferably placed at energy dispersion-free positions in the optical lattice. For example, in the AD it is located in a position with zero dispersion. This simplifies emittance measurements since one does not have to deal with dispersive components. However, unlike the AD, there is no position with zero dispersion along the ELENA lattice. This will require a careful analysis of the finite dispersion on the signal and the design of efficient algorithms taking it into account.

An additional challenge is the emittance measurement for non-Gaussian beams. In several facilities, where electron cooling is a fundamental part and diffusion effects (rest gas and intrabeam scattering) are also important, the beam can adopt highly non-Gaussian beam distributions. For instance, beam profile measurements in the AD in the past [9] have shown non-Gaussian transverse beam distributions with a very dense core and long amplitude tails, generated during the beam cooling process (stochastic and electron cooling). In recent years such a core-tail beam structure in the AD has been confirmed using Gas Electron Multiplier (GEM) based beam profile monitors [10,11].

---

[*] Corresponding author.
E-mail address: james.hunt@cockcroft.ac.uk (J.R. Hunt).

https://doi.org/10.1016/j.nima.2018.04.018
Received 2 January 2018; Received in revised form 6 April 2018; Accepted 9 April 2018

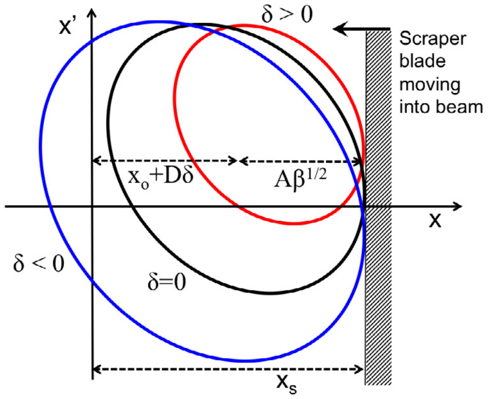

Fig. 1. Schematic of a scraper blade moving horizontally into a beam. The ellipses represent the acceptances for a beam with zero momentum offset (black), with positive momentum offset (red) and with negative momentum offset (blue). (For interpretation of the references to colour in this figure legend, the reader is referred to the web version of this article.)

After describing the principle of emittance measurements by scraping in Section 2, in Section 3 we briefly describe an algorithm for the particular case of Gaussian beams and propose an algorithm to calculate the emittance for arbitrary beam distributions. Simulations of emittance measurement by scraping in ELENA are shown in Section 4, followed by an analysis of various sources of errors. Finally, in Section 5 we draw some conclusions and plan for further studies.

2. Emittance measurements by scraping

In the algorithms developed below, we seek to determine the RMS value of the geometric transverse emittance, which may be defined statistically as:

$$\epsilon_{rms} = \langle J \rangle \equiv \frac{1}{2}\langle A^2 \rangle \tag{1}$$

where A is the amplitude of the particles in phase space, and J the action variable.

The principle of emittance measurements by scraping is based on a limiting aperture moving slowly into the beam to progressively remove the beam particles. Here, we consider the example of a metallic scraper blade moving slowly (compared to the revolution frequency) into the beam. Let us assume that the scraper aperture movement is slow enough such that the remaining beam intensity can be safely approximated by the fraction of the beam particles within the acceptance defined by the scraper position. Fig. 1 is a phase space plot to illustrate a horizontal scraper blade approaching the beam from the positive x-axis with a positive dispersion D.

Let us consider the normalised betatron phase space:

$$X_\beta = \frac{x_\beta}{\sqrt{\beta}}, \qquad X'_\beta = x'_\beta\sqrt{\beta} + \frac{x_\beta \alpha}{\sqrt{\beta}}, \tag{2}$$

where x_β and x'_β are the non-normalised particle betatron position and divergence angle in the beam, respectively, and β and α are the Twiss parameters in the corresponding transverse plane. The normalised amplitude in phase space is then given by $A = \sqrt{X_\beta^2 + X_\beta'^2}$, i.e.

$$A \equiv \sqrt{2J} = \sqrt{x_\beta^2\gamma + 2x_\beta x'_\beta\alpha + x_\beta'^2\beta}, \tag{3}$$

with $\gamma \equiv (1+\alpha^2)/\beta$ and J the action variable. The subindex "β" refers to the betatron component of phase space. If at the scraper position the first order dispersion is $D \neq 0$ and we assume a relative particle momentum offset $\delta \equiv \Delta p/p$, then the total position and angle can be written in terms of the betatron and dispersive contributions as $x = x_0 + x_\beta + D\delta$ and $x' = x'_0 + x'_\beta + D'\delta$, respectively, with $D' = \mathrm{d}D/\mathrm{d}s$. A displacement (x_0, x'_0) with respect to the reference closed orbit is also assumed.

A relative momentum offset $\delta > \delta_{max} := (x_s - x_0)/D$ corresponds to a closed orbit inside the scraper blade at position x_s; thus the transverse acceptance for parts of the initial beam with $\delta > \delta_{max}$ vanishes. For relative momentum offsets $\delta < \delta_{max}$, the transverse acceptance is determined by the distance $x_s - (x_0 + D\delta)$ between the momentum dependent closed orbit $(x_0 + D\delta)$ and the scraper position x_s. The acceptance for lower (higher) momentum offset δ corresponding to the blue (red) ellipse in Fig. 1 is larger (smaller) than for on-momentum particles (black ellipse).

The maximum oscillation amplitude defining the transverse acceptance is a function of the momentum offset given by:

$$A_{max} = \begin{cases} \dfrac{x_s - x_0 - D\delta}{\sqrt{\beta}} & \text{for } \delta < \delta_{\max}, \\ 0 & \text{otherwise.} \end{cases} \tag{4}$$

For the sake of clarity, the resulting acceptance in longitudinal and transverse phase space is depicted in Appendix A (Fig. A.18).

In general, before scraping a beam can be characterised by a distribution density:

$$\rho(\delta, A) = \rho_p(\delta)\rho_{\mathrm{T}}(\delta, A), \tag{5}$$

where the total density $\rho(\delta, A)$ can be represented as the product of two densities: the synchrotron amplitude distribution $\rho_p(\delta)$, expressed as a function of the relative momentum offset δ, and the transverse amplitude distribution $\rho_{\mathrm{T}}(\delta, A)$, which depends on A and intrinsically on δ through the dispersive component of the position.

The phase space density is normalised as follows:

$$\int_{-\infty}^{+\infty} \mathrm{d}\delta \rho_p(\delta) = 1, \tag{6}$$

$$\int_0^{+\infty} \mathrm{d}A 2\pi A \rho_{\mathrm{T}}(\delta, A) = 1. \tag{7}$$

Here, we will further assume the case of a coasting beam (the measurement of the emittance by scraping of a bunched beam may be more complicated) and no transverse plane (x–y) cross-coupling.

Taking into account the acceptance limits above, the remaining fraction of the beam in the machine with dispersion $D > 0$ is determined by the following integral:

$$F_+(x_s) = \frac{N_+(x_s)}{N_0} = \int_{-\infty}^{\delta_{max}} \mathrm{d}\delta \rho_p(\delta) \int_0^{A_{max}} \mathrm{d}A \; 2\pi \; A \; \rho_{\mathrm{T}}(\delta, A), \tag{8}$$

where N_0 is the number of particles in the machine before scraping and $N_+(x_s)$ is the number of particles left in the machine when the scraper is at x_s.

Similarly, if the scraper is coming from the negative x-axis, we obtain:

$$F_-(x_s) = \frac{N_-(x_s)}{N_0} = \int_{\delta_{max}}^{+\infty} \mathrm{d}\delta \rho_p(\delta) \int_0^{-A_{max}} \mathrm{d}A 2\pi A \rho_{\mathrm{T}}(\delta, A). \tag{9}$$

The integrals above give the cumulative distribution functions (CDF) of the beam loss. With this information one can obtain the corresponding probability density functions (PDF) projected on x_s from the derivatives $f_\pm = \pm \mathrm{d}F_\pm(x_s)/\mathrm{d}x_s$,

$$f_+(x_s) = \int_{-\infty}^{\frac{x_s - x_0}{D}} \mathrm{d}\delta \rho_p(\delta) 2\pi \frac{x_s - D\delta - x_0}{\beta} \times \rho_{\mathrm{T}}\left(\delta, \frac{x_s - D\delta - x_0}{\sqrt{\beta}}\right), \tag{10}$$

$$f_-(x_s) = \int_{\frac{x_s - x_0}{D}}^{+\infty} \mathrm{d}\delta \rho_p(\delta) 2\pi \frac{D\delta + x_0 - x_s}{\beta} \times \rho_{\mathrm{T}}\left(\delta, \frac{D\delta + x_0 - x_s}{\sqrt{\beta}}\right). \tag{11}$$

An example of a CDF and its corresponding PDF for a Gaussian distribution is shown in Fig. 2. Details of the derivation of the function f_+ from F_+ are shown in Appendix A.

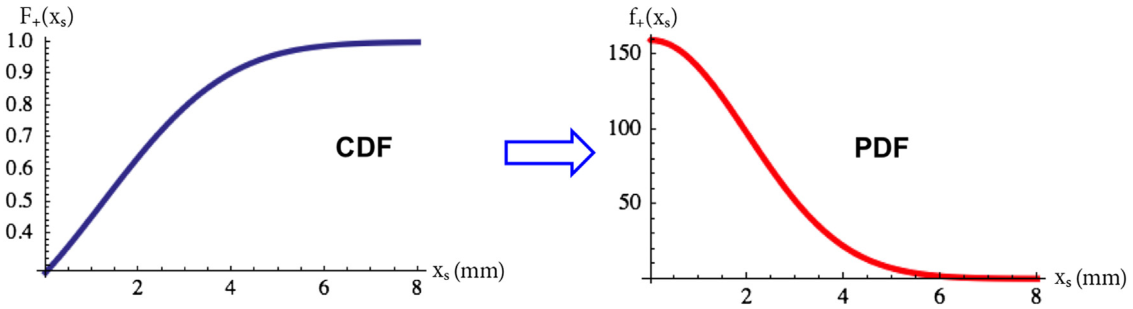

Fig. 2. Example of a cumulative distribution function (left) and its corresponding probability density function (right) for a Gaussian distribution.

3. Emittance reconstruction algorithm

3.1. Gaussian beams

If the beam passing the scraper in a dispersive region is known to have a Gaussian distribution, the beam density (Eq. (5)) is determined by:

$$\rho_p(\delta) = \frac{1}{\sqrt{2\pi}\sigma_\delta} e^{-\frac{\delta^2}{2\sigma_\delta^2}} \quad \text{and} \quad \rho_{\rm T}(\delta, A) = \frac{1}{2\pi\epsilon_{\rm rms}} e^{-\frac{A^2}{2\epsilon_{\rm rms}}}, \tag{12}$$

where the average momentum offset has been set to zero, $\langle\delta\rangle = 0$, and A is given by Eq. (3). Substituting Eq. (12) into Eqs. (8) and (9), and after solving the corresponding integrals, one obtains:

$$\begin{aligned} F_\pm(x_s) = {} & \frac{1}{2}\left[1 \pm \operatorname{erf}\left(\frac{A_0}{\sqrt{2\epsilon_{\rm rms}}|d|}\right)\right] \\ & - \frac{1}{2\sqrt{1+d^2}} e^{-\frac{A_0^2}{2(1+d^2)\epsilon_{\rm rms}}} \left[1 \pm \operatorname{erf}\left(\frac{A_0}{\sqrt{2\epsilon_{\rm rms}}|d|\sqrt{1+d^2}}\right)\right], \end{aligned} \tag{13}$$

where $A_0 = (x_s - x_0)/\sqrt{\beta}$ and $d = D\sigma_\delta/\sqrt{\beta\epsilon_{\rm rms}}$, and $\operatorname{erf}(x) = \frac{2}{\sqrt{\pi}}\int_0^x {\rm d}t\, e^{-t^2}$ is the so-called error function.

Then, for the probability density functions we obtain:

$$\begin{aligned} f_\pm(x_s) = {} & \frac{d}{\sqrt{2\pi\beta\epsilon_{\rm rms}(1+d^2)}} e^{-\frac{A_0^2}{2\epsilon_{\rm rms}d^2}} \\ & \pm \frac{A_0 e^{-\frac{A_0^2}{2(1+d^2)\epsilon_{\rm rms}}}}{2(1+d^2)^{3/2}\sqrt{\beta\epsilon_{\rm rms}}} \left[1 \pm \operatorname{erf}\left(\frac{A_0}{\sqrt{2\epsilon_{\rm rms}}|d|\sqrt{1+d^2}}\right)\right]. \end{aligned} \tag{14}$$

Note that the absolute value $|d|$ in the argument of the error function arises from the fact that changing the sign of the dispersion does not alter the result (exchange particles with positive and negative momentum offset).

3.2. General case algorithm

In order to compute the rms emittance value for arbitrary beam distributions, first we express the second moment of $(x_s - x_r)$ in terms of density functions $f_\pm(x_s)$, Eqs. (10) and (11), with the variable x_r being an estimate for the central orbit coordinate x_0. We may develop the cases for the scraper blades coming from the positive and negative x_s-axis simultaneously:

$$\langle(x_s - x_r)^2\rangle_\pm = \int_{-\infty}^{+\infty} {\rm d}x_s (x_s - x_r)^2 f_\pm(x_s) = \bar{x}_\pm^2 + \sigma_\pm^2 - 2\bar{x}_\pm x_r + x_r^2, \tag{15}$$

where $\langle\ldots\rangle$ denotes the expectation value of the quantity in the parenthesis and

$$\int_{-\infty}^{+\infty} {\rm d}x_s x_s^2 f_\pm(x_s) = \bar{x}_\pm^2 + {\sigma_\pm}^2, \tag{16}$$

$$\int_{-\infty}^{+\infty} {\rm d}x_s x_s f_\pm(x_s) = \bar{x}_\pm, \tag{17}$$

$$\int_{-\infty}^{+\infty} {\rm d}x_s f_\pm(x_s) = 1, \tag{18}$$

where $\bar{x}_\pm$ is the mean value of the measured distribution and $\sigma_\pm$ is the rms measured beam size. We may also write this quantity in terms of the emittance:

$$\begin{aligned} \langle(x_s - x_r)^2\rangle_\pm = {} & (x_0 - x_r)^2 + D^2(\bar{\delta}^2 + {\sigma_\delta}^2) + 2\beta\epsilon_{rms} + 2(x_0 - x_r)D\bar{\delta} \\ & \pm 2(x_0 - x_r)\sqrt{\beta}\bar{A} \pm 2D\sqrt{\beta}\langle\delta A\rangle. \end{aligned} \tag{19}$$

Summing terms for positive and negative scraper scans in Eqs. (15) and (19) we may write:

$$\begin{aligned} & \langle(x_s - x_r)^2\rangle_+ \\ & + \langle(x_s - x_r)^2\rangle_- = 2(x_0 - x_r)^2 + 2D^2(\bar{\delta}^2 + {\sigma_\delta}^2) + 4\beta\epsilon_{rms} + 4(x_0 - x_r)D\bar{\delta} \\ & \qquad = \bar{x}_+^2 + \bar{x}_-^2 + {\sigma_+}^2 + {\sigma_-}^2 - 2x_r(\bar{x}_+ + \bar{x}_-) + 2x_r^2. \end{aligned} \tag{20}$$

which may arranged and simplified to find an expression for ϵ_{rms} (see Appendix B for a more detailed explanation of this derivation):

$$\epsilon_{rms} = \frac{1}{4\beta}\left[\sigma_+^2 + \sigma_-^2 + \frac{(\bar{x}_+ - \bar{x}_-)^2}{2}\right] - \frac{D^2\sigma_\delta^2}{2\beta}, \tag{21}$$

which contains only values that can be obtained from the scraper data or otherwise measured and estimated, and hence forms the basis of the algorithm.

Eq. (21) shows explicitly the subtraction of the dispersive term depending on the momentum spread. Similarly, we can proceed in the same way for the vertical plane, where generally $D = 0$.

The calculation of the emittance applying the above method requires a complete scan on both the negative and positive side of the x_s coordinate, i.e. two measurements. This requires two machine cycles, and therefore the stability of the machine during the measurement process is very important.

The main problem is how to obtain the information of the functions $f_\pm(x_s)$. The curves $F_\pm(x_s)$ are obtained from discrete data by scraping and, in general, we will not know the mathematical expression that better fits such curves. Therefore, unless we have any information a priori on the shape of the beam distribution, it will not be possible to apply symbolic differentiation. In this case, first we need to apply numerical interpolation of the recorded $F_\pm$ data, and then numerical differentiation to obtain $f_\pm$.

For instance, given the tabulated function $F_\pm$ we can use cubic spline interpolation [12]. One of the main advantages of spline interpolation over polynomial interpolation is that it leads to small interpolation errors even when low degree polynomials are used for the spline. In addition, applying spline interpolation we can avoid the so-called

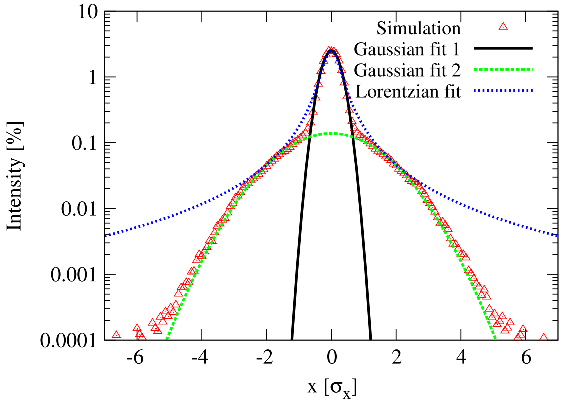

Fig. 3. Example of horizontal antiproton beam distribution after 8 s e-cooling, including also IBS effects, at 35 MeV/c momentum. The horizontal axis is normalised to the initial rms width. The red triangles show the result of the BETACOOL simulation. Gaussian fittings to both the dense core (black solid line) and the tails (dashed green line) are also shown. In addition, a Lorentzian function fitting has also been performed (dotted blue line).

Runge's phenomenon, which is a problem of oscillation between equispaced points that occurs when using polynomial interpolation with high degree polynomials [13].

Given that the detectors will have a high data acquisition rate, we may alternatively forgo the spline and use more basic approximations to determine $f_{\pm}$. An investigation to compare the accuracy of spline interpolation with simple numerical methods was carried out. It was found that there was a negligible difference between the two, assuming a data acquisition rate of 400 Hz. The results can be seen in Appendix C, along with an explanation of the methods used.

4. Simulations

4.1. Expected beam profiles in ELENA

To simulate the cooling process and the beam parameter evolution during cooling we have used the code BETACOOL [14], which allows us to perform long-term multiparticle tracking simulations, including several cooling and heating processes affecting the beam. The code BETACOOL has been benchmarked with measurements in the past, for example in the context of the low energy ion ring ELISA [15], giving a reasonable agreement.

In ELENA, e-cooling is applied at three stages of the machine cycle: after deceleration ramps, at p = 35 MeV/c and 13.7 MeV/c, respectively, for a coasting beam; and during bunching prior to ejection at 13.7 MeV/c.

A typical core-tail beam distribution obtained after the simulation of the cooling process in presence of heating diffusion effects is shown in Fig. 3. It presents a dense core and long tails, which can be well represented by a bi-Gaussian function in a broad dynamic range. The central region ($-3\sigma_x < x < 3\sigma_x$) can also be well described by heavy-tailed functions, such as a Lorentz function or a Lévy stable symmetrical distribution. A more extensive discussion can be found in [16].

4.2. Scraping process in ELENA

In ELENA, two aluminium scraper windows (Fig. 4) (one horizontal, one vertical) will be used to scrape the beam from four directions [7]. A combination of scintillators and four in-vacuum multichannel plate (MCP) detectors will be used to measure the intensity of the secondary particle showers produced when particles collide with the scraper blade. From this data the beam intensity as a function of the scraper position can be inferred.

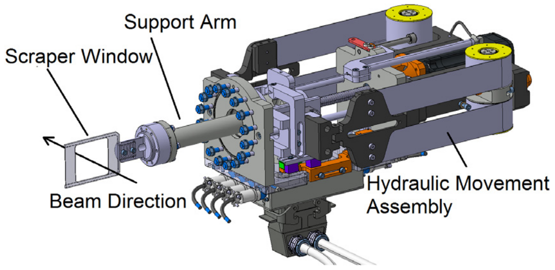

Fig. 4. A model of the horizontal scraper blade window in the extended position for use in ELENA [17].

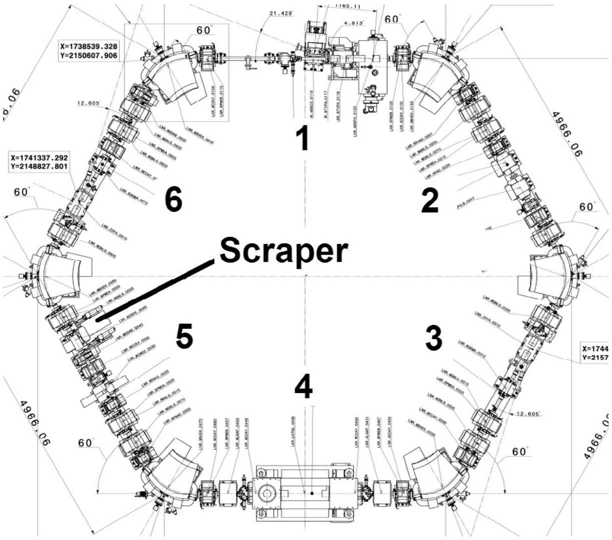

Fig. 5. Schematic diagram of ELENA highlighting the six section names and the position of the scraper system.

Table 1
ELENA scraper system parameters.

Parameters	Specifications
Material	Aluminium
Max. scraper movement	±40 mm
Scraper Window Diameter	66 mm
Movement precision (step)	0.1 mm
Frequency of acquisition	400 steps/s

Some relevant ELENA scraper system parameters are summarised in Table 1.

This scraper system is placed in Section 5 of the ELENA lattice (Fig. 5), which in the context of the simulations presented here, gives the following optics parameters for the position of the horizontal scraper blade: $\beta_x \approx 0.69$ m, $\beta_y \approx 3.00$ m, $\alpha_x \approx -0.74$, $\alpha_y \approx -0.30$, $D_x \approx 1.30$ m.

In order to simulate the scraping process, we have implemented a rectangular limiting aperture into the MAD-X [18] ELENA lattice model. Here, this element acts as a perfect collimator, i.e. particles with position amplitude larger than the aperture are considered lost. At this stage of the simulation, no interaction of the beam with the scraper material is being introduced. The element can be moved transversally along the x and y axes, allowing it to emulate the scraper blade windows.

Then, multi-turn and multiparticle tracking along the ring is simulated using the Polymorphic Tracking Code (PTC) module in MAD-X [18]. Considering the beam parameters corresponding to the stage of the machine cycle that we want to simulate, an initial distribution of 10^4 macro-particles, representing an intensity of 2.5×10^7 antiprotons, is tracked for several tens of thousands of turns.

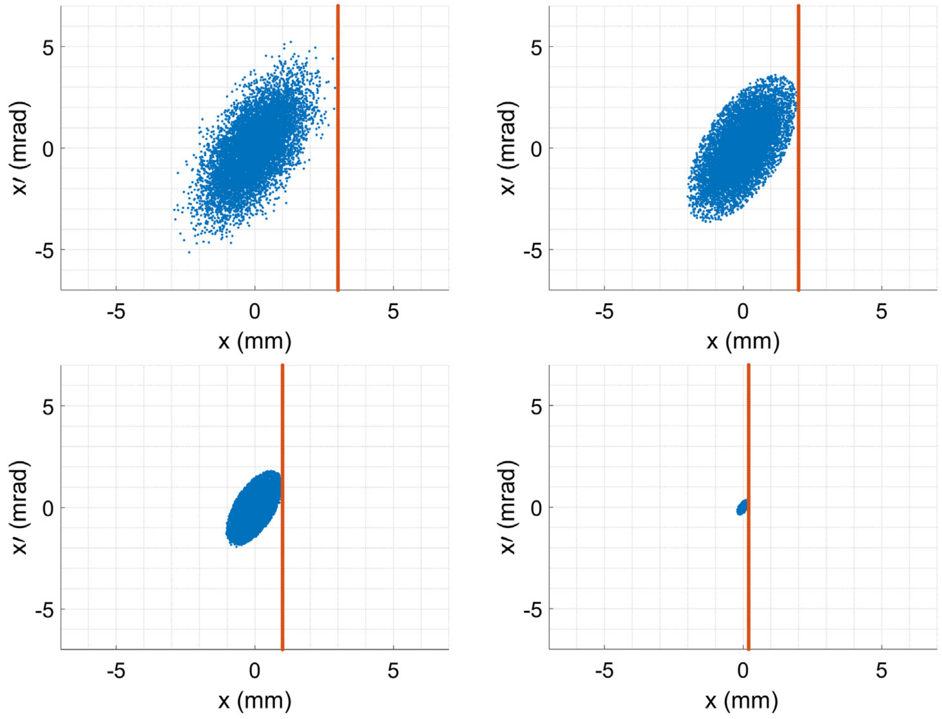

Fig. 6. Horizontal phase space at different scraper measurement stages for an on-momentum Gaussian beam. The red line indicates the position of the scraper blade.

Firstly we have assumed an ideal case, where the scraper element is well centred with respect to the nominal orbit, and no imperfections in the ELENA optics. Then the scraper is moved into the beam by applying a misalignment to the scraper element. Following the conventions of previous sections, as in Fig. 1, let us just assume a scraper scan in the positive x_s-axis.

To simplify the simulations, the continuous movement of the scraper has been replaced by a step-wise movement. After 370 revolutions the scraper edge position was decreased by 0.1 mm. This corresponds, on average, to the nominal scraper speed of 40 mm/s with a 100 keV beam. Every particle with a larger position than the edge of the scraper blade was removed from the simulation and the phase space co-ordinates and number of particles remaining after each 0.1 mm step were recorded to reconstruct the cumulative function $F_+(x_s)$.

To illustrate the scraping process, Fig. 6 shows the horizontal phase space for different measurement times (different blade positions).

4.3. Scraping results analysis

For thoroughness and to test the simulation was working properly, the results from a Gaussian beam simulation were first analysed using the Gaussian beam only algorithm discussed in Section 3. Fig. 7 shows the results of this analysis for several simulations with varying input beams. The scraper blade was moved through the beam from positive x once for each simulation to obtain $F_+(x_s)$. The expression obtained previously was fit to the data to give reconstructed values for the emittance and momentum spread.

For the four beams that were run, the algorithm returned values within 7% of the input emittances, including for beams with relatively large momentum spreads. The error may be attributed to the statistical nature of the simulations, and due to the discrete scraper steps of 0.1 mm. Additionally, taking the longitudinal momentum spread, σ_δ, as a second free parameter enabled the algorithm to estimate this value simultaneously at some cost of emittance value accuracy. The results confirm that the single scan algorithm works for Gaussian beams for within a chosen accuracy limit of 10%. The two scan arbitrary distribution algorithm was tested next.

Fig. 8(a) and (b), show the results of scraper scans from positive and negative x taking the most simple case: a beam with Gaussian distributions in transverse phase space, zero momentum spread, σ_δ, and a transverse emittance (ϵ_x, ϵ_y) of 1 mm mrad. The input ϵ_x was calculated upon beam generation using the phase space parameters of all particles to be 0.9987 mm mrad. The value given by the algorithm after running the beam through the simulation was 0.9930 mm mrad, a difference of 0.57% which could be attributed to statistical fluctuations. This is, however, the simplest possible case, and so further simulations were run to test the robustness of the algorithm.

The process was repeated (Fig. 8(c) and (d)) for a bi-Gaussian beam with the same parameters. The emittance ϵ_x obtained from the macro-particle distribution was 1.004 mm mrad. The resultant output emittance was 1.012 mm mrad resulting in a negligible difference of 0.83%. Successful scans in x with zero momentum spread confirm that the algorithm will work when scanning in y, as $D_y = 0$ around the ring.

The simulations were repeated for both beam distributions with non-zero values of momentum spread ranging from $\sigma_\delta = 1 \times 10^{-4}$ to $\sigma_\delta = 1 \times 10^{-3}$ and a range of input emittances ϵ_x from 0.4 mm mrad to 10 mm mrad. The results show that the error remains below 2.4% in all cases tested, confirming the versatility of the algorithm. The data may be found in Appendix D.

An example of the resultant CDF is shown in Fig. 8(e) and (f), the effect of the longitudinal momentum spread can be seen as the curves do not drop to zero at the centre of the closed orbit, $x_0 = 0$. A comparison of plots (e) and (f) with (c) and (d) shows how much the momentum spread can affect the CDF, and why the double scraper scan method is necessary for non-Gaussian beams. A clear demonstration of the effect can seen in Fig. 9 where simulations were used to plot the phase space ellipses of particles with and without momentum spread.

The simulations presented so far assume that a perfect estimation of the longitudinal momentum spread has been supplied to the algorithm. In practice this will not be the case and a further investigation into this and other systematic errors was performed.

4.4. Systematic errors

As the scraping algorithm is designed to work with a low intensity coasting beam, Schottky diagnostics will be used to estimate the

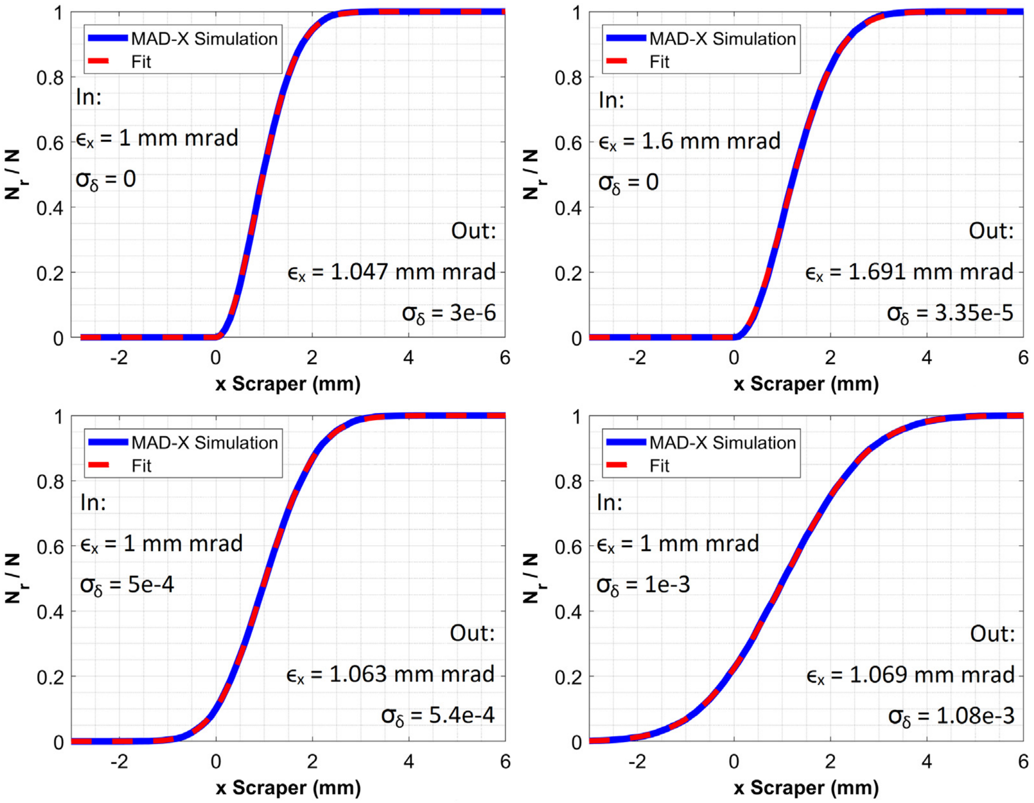

Fig. 7. Intensity data for beams of varying parameters overlaid with the Gaussian algorithm fit.

longitudinal momentum spread. As a result, the rms momentum offset value given to the algorithm may be inaccurate, with an error of up to around 20%. To investigate the effect this may have on the reconstructed emittance value, the algorithm was used with varying degrees of incorrect momentum offset.

Eq. (21) was rearranged to obtain an estimation for the errors:

$$\frac{\Delta\epsilon_{rms}}{\epsilon_{rms}} = \frac{-1}{2\beta} D^2 \sigma_\delta{}^2 \left(2\left(\frac{\Delta\sigma_\delta}{\sigma_\delta}\right) + \left(\frac{\Delta\sigma_\delta}{\sigma_\delta}\right)^2\right)\frac{1}{\epsilon_{rms}}, \tag{22}$$

which were plotted with the simulation results (Fig. 10).

For a more realistic momentum spread ($\sigma_\delta = 3\times10^{-4}$), the algorithm can tolerate errors of up to 20% for a lower emittance beam, and even greater for larger beams. When performing the study for a beam with a larger momentum spread ($\sigma_\delta = 1\times10^{-3}$), the algorithm was much more sensitive to momentum spread errors. It can be seen that even for a larger sized beam, an error greater than 5% could result in an emittance error over the desired value (10%). It should be noted that due to statistical fluctuations, there is already a small error on the measurements for an accurate momentum offset reading.

A further source of error was investigated by introducing a non-zero closed-orbit offset. Since the algorithm relies on calculating the area underneath the PDF and the relative position of the PDFs between the two scraper scans, it is not affected by a closed orbit offset — so long as the offset is consistent between the two scraper scans. As expected the results of the simulation were identical to those obtained for a beam with $x_0 = 0$.

In a more realistic scenario, the closed orbit of the beam may change during each run of the machine. To study how this would impact the accuracy of the algorithm, the closed orbit was held at $x_0 = 0$ during scraper scans from positive x, and varied during scans from negative x. The results presented in Fig. 11 show that a difference in closed orbit of more than 0.1 mm could affect the reconstructed value of emittance by around 10% depending on the beam size.

Rearranging Eq. (21) to predict the closed orbit offset error yields:

$$\frac{\Delta\epsilon_{rms}}{\epsilon_{rms}} = \frac{-1}{8\beta}(2(\bar{x}_+ - \bar{x}_-)\Delta\bar{x}_- - (\Delta\bar{x}_-)^2)\frac{1}{\epsilon_{rms}}, \tag{23}$$

which was plotted against the data showing that the simulations behave as expected. Small differences may be due to the statistical nature of beam generation and this level of accuracy is adequate for these purposes.

This method of testing the closed orbit offset also reflects how the accuracy of the scraper blade position could affect the result. An error in the relative blade position (between the positive and negative scraper blades) is equivalent to a closed orbit offset. Similarly to the momentum offset error simulations there is a small error on the measurements for perfectly matched closed orbits.

In addition to closed orbit and scraper alignment errors, the accuracy of the estimation of β_x at the scraper position will affect the output from the algorithm. Similarly to the σ_δ error investigation, the algorithm was run with varying incorrect values of β_x for a range of input emittances. A theoretical estimation for the error was obtained by rearranging Eq. (21):

$$\frac{\Delta\epsilon_{rms}}{\epsilon_{rms}} = \left(1+\frac{\Delta\beta}{\beta}\right)^{-1} - 1. \tag{24}$$

The results can be seen in Fig. 12. Differently from errors in σ_δ and x_0, the magnitude of the emittance does not affect the impact of an error in β_x, looking at Eqs. (21) and (24) we can see this is simply because the value returned is inversely proportional to β_x and does not depend on ϵ_{rms}. The theoretical prediction agrees extremely well with the simulation data.

Taking a lattice with $\beta_x = 0.69$ m at the horizontal scraper blade, we can see that the algorithm can tolerate an error of $-8\% \lesssim \Delta\beta_x \lesssim 11\%$, for our target accuracy of 10% reconstructed value.

A study investigating the effects of a tilt misalignment of the scraper blades was performed. Since opposing scraper blades are connected to

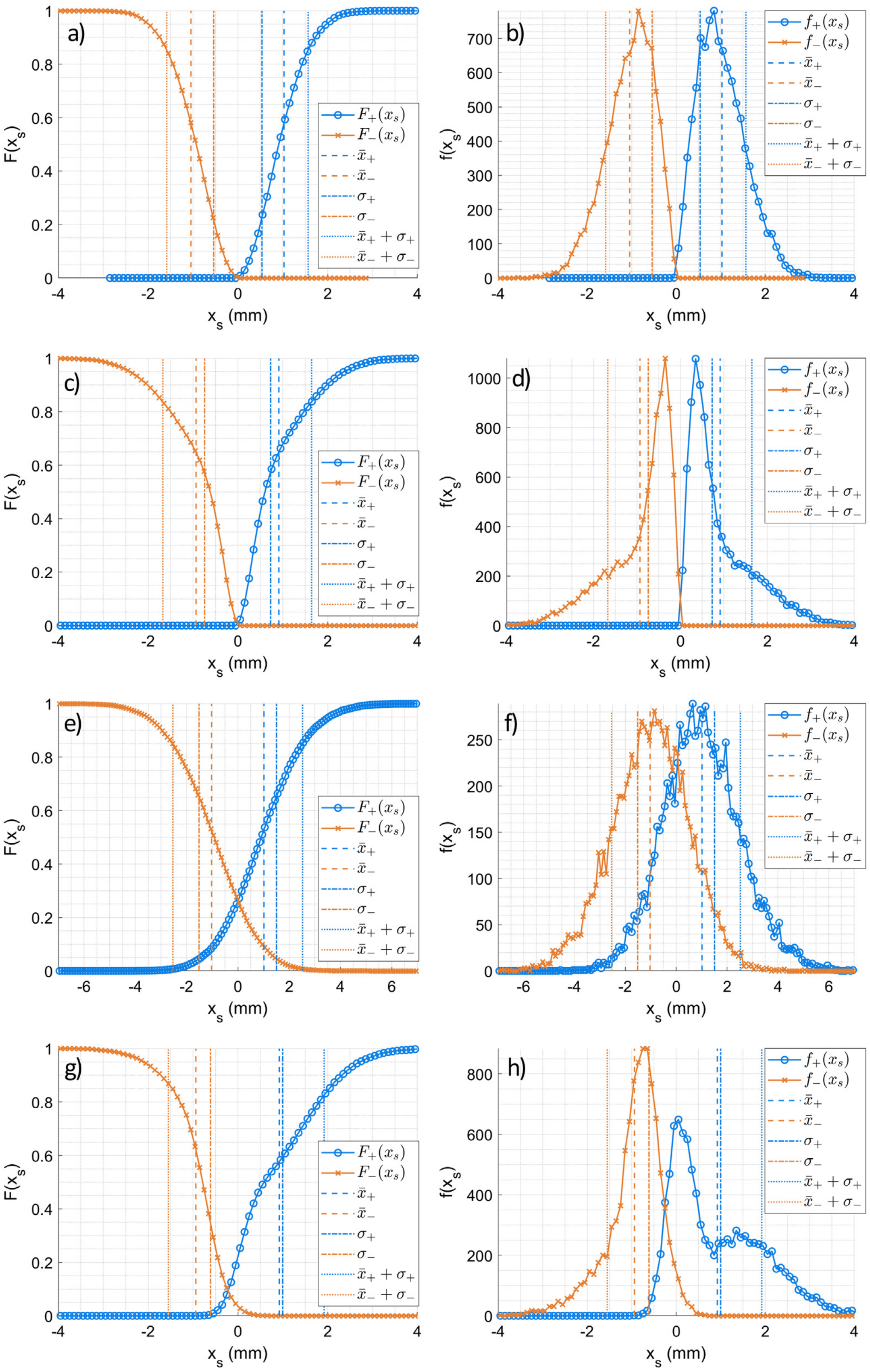

Fig. 8. Cumulative distribution of beam with spline fitted for scraper coming from both positive and negative x, $F_\pm$ (left plots), and the reconstructed probability density of beam, $f_\pm$, derived from the differentiated spline (right plots). (a) and (b), and (c) and (d) show results for Gaussian and bi-Gaussian beams, respectively. Both have $\epsilon_x = 1$ mm mrad and $\sigma_\delta = 0$. Plots (e) and (f) show the results from a bi-Gaussian beam with $\epsilon_x = 1.2$ mm mrad and $\sigma_\delta = 1 \times 10^{-3}$. Finally, plots (g) and (h) display the results for a bi-Gaussian beam which has a correlation between momentum spread and emittance (discussion in Section 4.5).

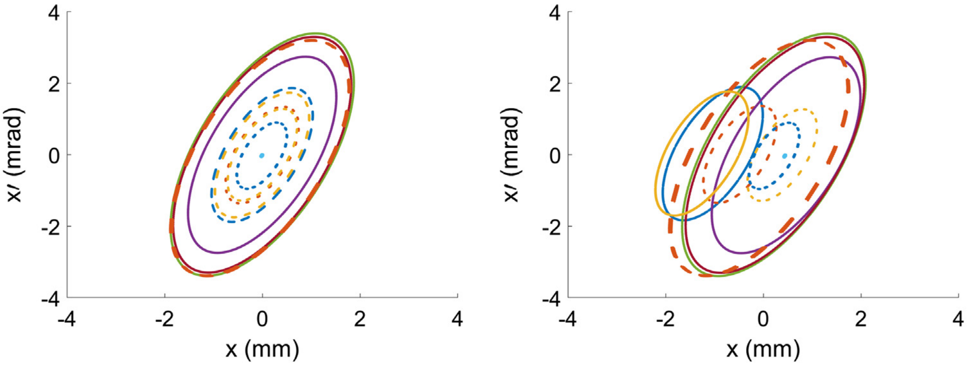

Fig. 9. Phase space ellipses for ten particles with zero (left plot) and non-zero (right plot) momentum offset in a dispersive region. It is clear that two beams with the same emittance but different momentum spreads yield different scraping profiles.

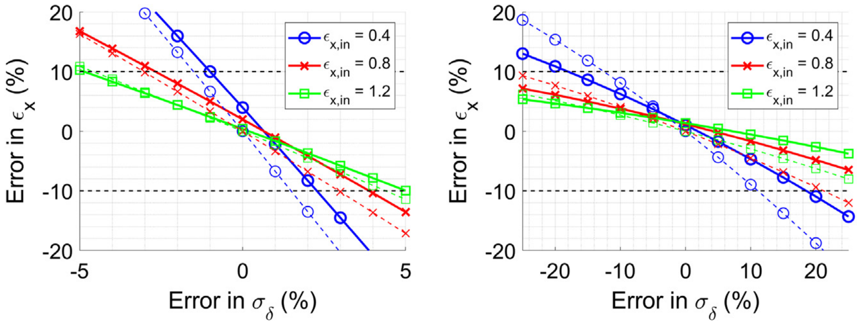

Fig. 10. Error in reconstructed emittance value as the result of varying the error in the estimation of rms momentum spread. The left plot shows the results for beams with $\sigma_\delta = 1 \times 10^{-3}$ and the right plot for $\sigma_\delta = 3 \times 10^{-4}$. Theoretical estimations for these errors are represented by dashed lines.

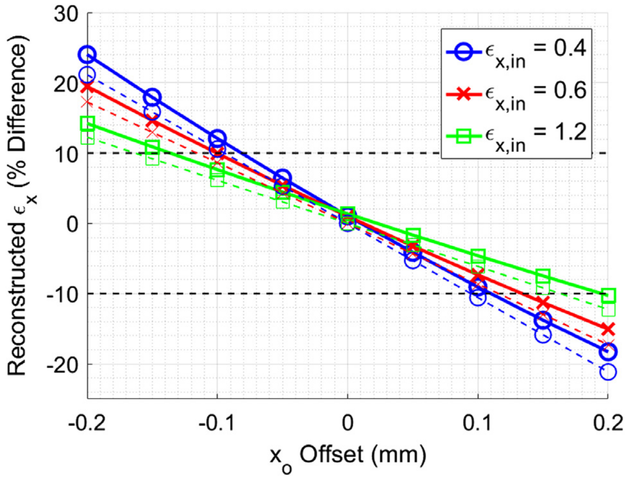

Fig. 11. Reconstructed horizontal emittances resulting from mismatched closed orbits between positive and negative scraper scans, for varying input emittances. The input bi-Gaussian beam had a realistic momentum spread of $\sigma_\delta = 3 \times 10^{-4}$. Theoretical estimations for these errors are represented by dashed lines.

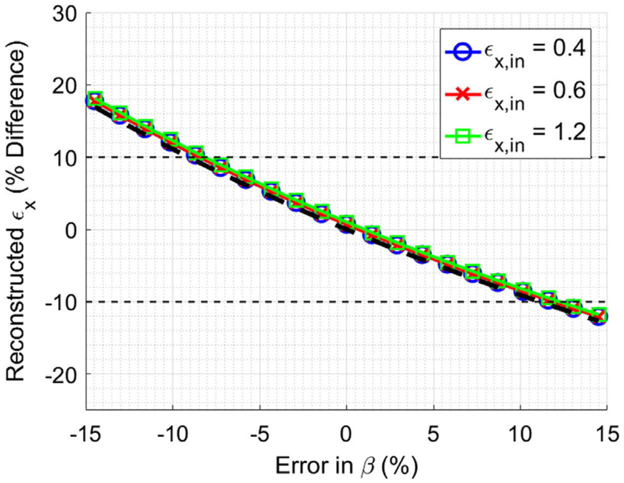

Fig. 12. The effects of incorrect estimations of β_x at the scraper position on the reconstructed emittance values. The input bi-Gaussian beam had a realistic momentum spread of $\sigma_\delta = 3 \times 10^{-4}$. The theoretical prediction is represented by a dashed line.

each other in the form of a window (Fig. 4), a tilt of the same magnitude was applied to the blades from both sides. For easy comparison of x and y a beam with no momentum spread was run in both cases, eliminating the influence of dispersion in x. Performing the simulations in x for a beam with $\sigma_\delta = 0.03\%$ showed a negligible difference in the reconstructed emittance values compared with zero momentum spread.

Fig. 13 shows the results of the simulation. A clear trend can be seen for scraping in both x and y, and negligible statistical fluctuations in the data allow simple polynomial fits. A theoretical estimation of the impact of this error was not calculated due to the complex nature of considering four dimensions in phase space instead of two as for the previous errors.

The results show that for a nominal beam in ideal conditions, the limits for a tilt error on the scraper blades in x and y are $\approx 1.95°$ and $\approx 10.3°$, respectively. The difference in the magnitude of the effect is due to the β parameters at the scraper, $\beta_{x,y} = 0.688, 3.001$ m. Comparing ratios, $\frac{\beta_x}{\beta_y} = 0.23$ and $\frac{1.95°}{10.3°} = 0.19$, suggests this effect could scale linearly with β.

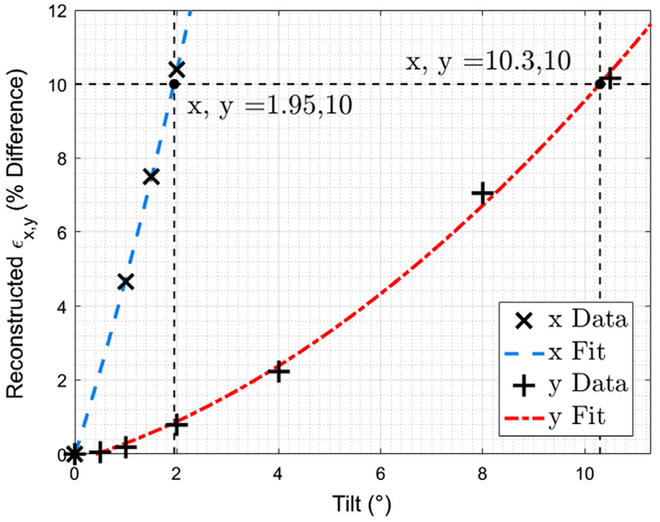

Fig. 13. Scraper blade tilt error in x and y against emittance out for a bi-Gaussian beam with $\epsilon_x = 1$ mm mrad and $\sigma_\delta = 0$.

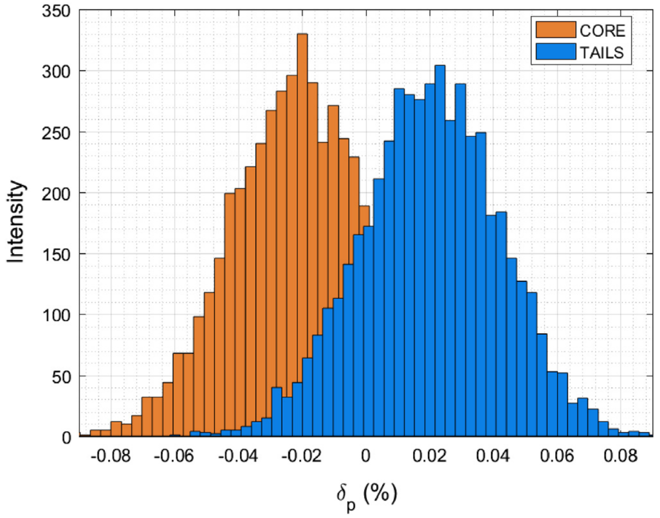

Fig. 14. Particle distribution of momentum offsets as an approximation for the effects of strong electron cooling. This beam has an average momentum difference, $\Delta\delta_p = 0.04\%$ between the core and tails, with an overall average $\delta_p = 0$. The σ_δ of the core and tails has been adjusted to give the overall distribution $\sigma_\delta = 0.03\%$.

4.5. Momentum–emittance correlation

During deceleration the beam will experience growth in transverse phase space. To counter these effects an electron cooler is applied during the cycle at two energy plateaus (0.65 MeV and 0.1 MeV). It is expected the distribution of transverse electron velocities, v_{e^-}, in the electron cooler will not be uniform and as a result a correlation between the betatron amplitude and particle momentum may appear in the beam. A parabolic distribution of v_{e^-} centred on $x, y = 0$ would give particles with greater emittance a larger momentum offset.

To test that the algorithm is capable of performing well under these circumstances a set of bi-Gaussian beams were generated as before, but with a different average δ_p for the core and tails. An example can be seen in Fig. 14. To investigate how the magnitude of such a correlation would impact the accuracy of the algorithm, all beams used in this study had the same input emittances $\epsilon_{x,y} = 1$ mm mrad, rms momentum offsets $\sigma_\delta = 0.03\%$, and average $\delta_p = 0$.

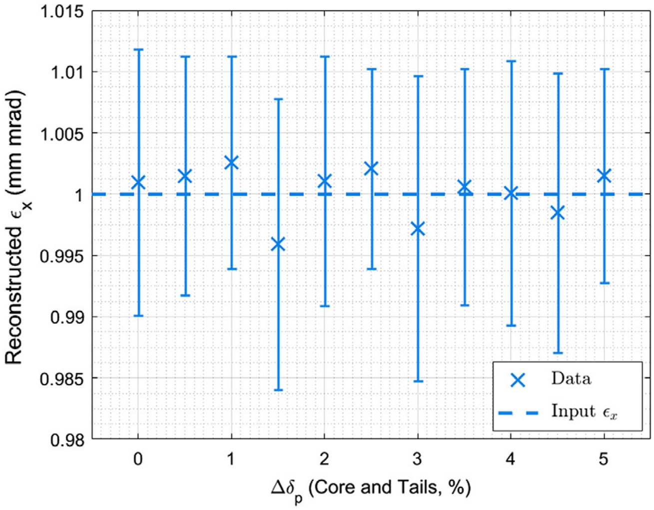

Fig. 15. The effect of increasing the correlation between momentum spread and emittance on the accuracy of the algorithm.

An example of the characteristic a-symmetric CDF and PDF due to this offset can be found in Fig. 8(g) & (h). A shift of the tails to positive x and core to negative x can be seen in F_+ and f_+ and is consistent with the difference in δ_p. Fig. 15 displays the impact on the resultant emittance as a function of the average momentum spread difference. Each point is the mean value taken from 20 simulations. Statistical fluctuations are observed, but no trend of increasing error can be seen as $\Delta\delta_p$ increases. The impact of the correlation on the accuracy of the algorithm can be seen as negligible because above the values of $\Delta\delta_p$ tested, the beam begins to appear unphysical in this approximation ($\Delta\delta_p \gg \sigma_{\delta,beam}$).

Additionally we can analytically compute a “correlation coefficient” which describes the magnitude of this effect in the beam:

$$\langle(\delta_p - \bar{\delta}_p)A\rangle = \frac{\sum_{i=1}^{2}(N_i\sqrt{\frac{\epsilon_{rms,i}\pi}{2}}(\bar{\delta}_i - \bar{\delta}_{beam})^2)}{\sum_{i=1}^{2} N_i}, \tag{25}$$

where subscripts $i = 1, 2$ represent the core and tail of the beam. In these simulations the beam is separated into two parts, however it would also be possible to have any number of parts to approximate a more continuous emittance–momentum spread correlation. We may reconstruct this correlation coefficient using quantities obtained during the scraping process:

$$\langle(\delta_p - \bar{\delta}_p)A\rangle = \frac{\sigma^2{}_+ + \sigma^2{}_-}{4D\sqrt{\beta}}. \tag{26}$$

Comparing the analytical and reconstructed results for different magnitudes of the correlation we see excellent agreement (Fig. 16). This coefficient provides further characterisation of the beam and could allow an investigation into the effects of the electron cooler.

Further studies to determine a realistic momentum spread profile in the presence of a non-uniform electron velocity distribution in the electron cooler will be performed using BETACOOL. This will provide a more realistic momentum offset distribution for further testing. However, the results presented here provide evidence that the algorithm is capable of accurately reconstructing the emittance in the presence of a correlation with momentum spread.

4.6. Diffusion effects

Diffusion effects during the scraper measurement may be other potential sources of systematic measurement errors, leading to an overestimate of emittance. Intra-Beam Scattering (IBS) and rest gas scattering

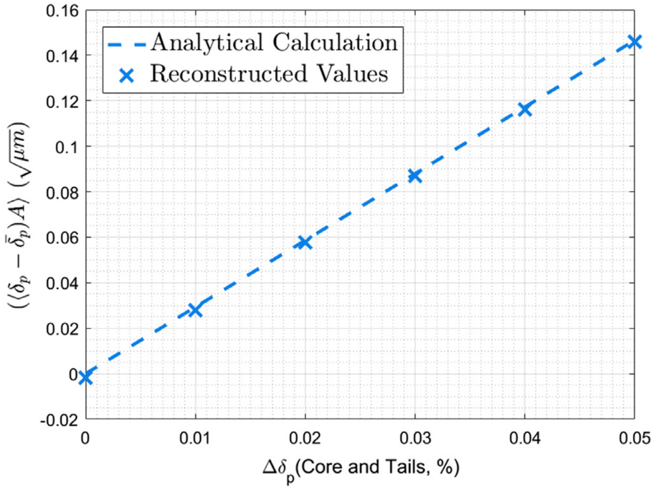

Fig. 16. A comparison of the analytical and reconstructed values of the correlation coefficient.

are amongst the most important blow-up and diffusion mechanisms for high density and low energy ion storage rings.

In the context of ELENA, assuming the nominal vacuum pressure of 3×10^{-12} Torr, the effect of rest gas scattering on the beam parameters has been estimated to be practically negligible in comparison with IBS [19]. So it is not considered relevant for the scraper performance in ELENA. However, IBS could be an important potential source of measurement error depending on the speed of the scraper with respect to the beam revolution frequency and the amplitude scan range. Diffusion growth of the emittance due to IBS could be significant in the case of relatively slow scans.

Let us briefly introduce IBS. It can be defined as a beam heating effect produced by multiple small-angle Coulomb scatterings of charged particles within the accelerator beam itself. It causes an exchange of energy between the transverse and longitudinal degree of freedom, thus leading to the growth of the beam phase space dimensions. The theory of IBS has been extensively described in the literature, e.g. [20–23], and many of these IBS models are implemented in the simulation code BETACOOL [14].

For a rough order of magnitude estimate of the IBS growth rates one can use the following proportionality expression:

$$\frac{1}{\tau_{x,y,p}} \propto \frac{r_p^2 c}{32\pi\sqrt{\pi}\beta^3\gamma^4\epsilon_x\epsilon_y\sigma_\delta}\cdot\lambda\,, \tag{27}$$

where $\lambda = N/C$ for coasting beams, and $\lambda = N_b/(2\sqrt{\pi}\sigma_s)$ for bunched beams. N is the total number of particles of the beam, N_b the number of particles in a bunch (for a bunched beam), σ_s the rms bunch length (for a bunched beam), C the circumference of the storage ring, r_p the classical proton radius, c the speed of light, β the relativistic velocity factor, γ the Lorentz factor ($\gamma \approx 1$ for low energy machines), $\epsilon_{x,y}$ the transverse emittances and σ_δ the relative momentum spread.

For the case of ELENA, IBS heating effects on the beam were extensively studied in [16,19,24]. Here, in order to illustrate the potential effect of IBS on the ELENA beam, we have just calculated the transverse emittance and momentum spread growths as a function of time.

In Eq. (27) we can see that IBS will be more critical at low energy (growth rate depends on $1/\gamma^4$), so we will focus on the study of the lowest kinetic energy in ELENA (100 keV). We have performed Monte Carlo tracking simulations using the model beam algorithm of BETACOOL and an initial distribution of 10^4 macro-particles representing 2.5×10^7 antiprotons. The following initial beam parameters at the equilibrium (after cooling) are assumed: $\epsilon_{x,y} = 1$ mm mrad and $\sigma_\delta = 5\times10^{-4}$. Then the transverse emittance and momentum spread growths due to IBS have been calculated as a function of time. To evaluate the IBS effects here we use the so-called Martini model [22], which is an extended version of Piwinski's model [20], taking into account lattice derivatives. The computation process can basically be summarised as follows: rms emittances and momentum spread are computed from the input macro-particle distribution; the growth rates are calculated at each element of the lattice along the ring, assuming Gaussian beams with these rms parameters; and, finally, random IBS kicks are then applied to the full macro-particle distribution based on the calculated growth rates.

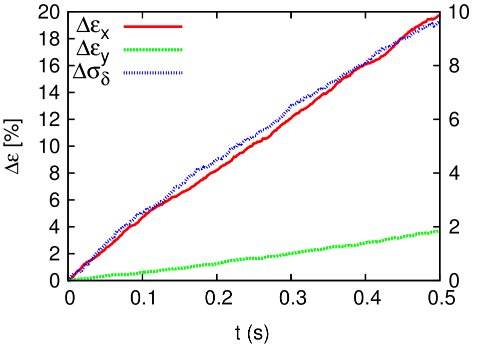

Fig. 17. Emittance and momentum spread increase due to IBS as a function of time in the ELENA ring for a coasting beam with 13.7 MeV momentum, assuming an initial equilibrium emittance of 1 mm mrad and relative momentum spread 5×10^{-4}.

Fig. 17 shows both transverse emittance and relative momentum spread growth in time due to IBS. It can give an estimate of the emittance growth from the end of the cooling process, where equilibrium has been achieved between cooling and IBS and the starting of the scraping process. Obviously, diffusion will become more important for lower scraper velocity, and therefore longer time steps. For example, to keep $\Delta\epsilon_x < 10\%$ the time lapse should be less than 300 ms.

The evaluation of the IBS impact during the scraper measurement is more complicate and requires taking into account the intensity reduction during scraping. Actually, the situation will become more favourable during the measurement progression, since the scraper will reduce the beam intensity in subsequent steps and IBS emittance growth rates will decrease according to $1/\tau_{x,y,p} \propto N$, as indicated in Eq. (27), where $N = N_0 \cdot F_\pm(x_s)$ is the number of remaining antiprotons in the beam.

5. Conclusions and prospects

We have developed algorithms for reconstructing the transverse emittances of beams in the dispersive region of a storage ring. The algorithms can reconstruct the emittance of a Gaussian beam using a single scraper scan, and with a combination of two successive measurements we can accurately reconstruct a beam of arbitrary particle distribution. The algorithms were developed for the ELENA ring but would also work for storage rings in other facilities.

The algorithms were successfully tested by simulations using a MAD-X model of the ELENA ring which is currently undergoing commissioning at CERN. For the two scan algorithm, we have considered various systematic errors that could affect the performance of the algorithm in operation, and determined mechanical error tolerances. Complications due to a correlation between emittance and momentum spread have been considered and we have shown the algorithm performs well in such circumstances, with the ability to accurately determine the magnitude of the correlation.

Additionally, effects generating diffusion such as intra-beam scattering may play a significant role in the performance of the algorithm given the low energies at which ELENA operates. In principle, IBS impact on emittance growth might be significant if operating in slow scan mode

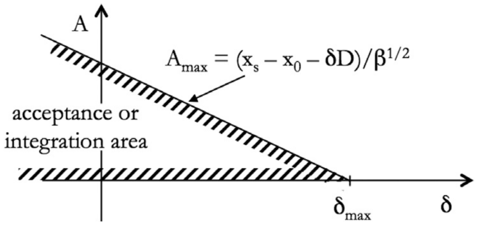

Fig. A.18. Integration area to compute the function F_+ estimating the fraction of particles for the scraper at position x_s.

and for an increased scan time due to large amplitude tailed beams. Simulation studies of the emittance performance measurement under the presence of IBS are ongoing.

Once ELENA is in full operation, we will take scraper data and compare results with those from our simulations as a benchmarking exercise. This will give us an insight into the effectiveness of our simulations, perhaps expose some additional unseen factors, and provide the context needed for these studies to be used in aid of the development of similar diagnostic devices in the future.

Finally, it is worth mentioning that we are also carrying out studies of less-invasive techniques for beam profile measurement and emittance reconstruction, based on ionisation profile monitors and supersonic gas jet monitors [1] adapted to low energy and low intensity hadron accelerators.

Acknowledgements

We gratefully acknowledge our colleagues from the ELENA team at CERN for very fruitful discussions.

This work is supported by the EU under Grant Agreement 624854 and the STFC Cockcroft Institute core Grant No. ST/G008248/1.

Appendix A. Derivation of probability density function f_+

The function F_+ given by Eq. (8) describes the fraction of particles inside the machine acceptance determined by an aperture at the position x_s, and is given by the density function integrated over the integration limits illustrated in Fig. A.18:

$$F_+ = \int_{-\infty}^{\delta_{max}} \mathrm{d}\delta n(\delta, x_s), \tag{A.1}$$

where $\delta_{max} = (x_s - x_0)/D$ and the density function $n(\delta, x_s)$ is defined as:

$$n(\delta, x_s) = \begin{cases} \rho_p(\delta) \int_0^{A_{max}} \mathrm{d}A 2\pi A \rho_\mathrm{T}(\delta, A) & \text{for } \delta \leq \dfrac{x_s - x_0}{D}, \\ 0 & \text{for} \delta > \dfrac{x_s - x_0}{D}, \end{cases} \tag{A.2}$$

where $A_{max} = (x_s - x_0 - D\delta)/\sqrt{\beta}$.

The density probability function f_+ defined as the derivative of F_+ with respect to x_s becomes:

$$f_+(x_s) = \frac{\mathrm{d}F_+(x_s)}{\mathrm{d}x_s} = \int_{-\infty}^{\frac{x_s - x_0}{D}} \mathrm{d}\delta \frac{\mathrm{d}n(\delta, x_s)}{\mathrm{d}x_s} + \frac{1}{D} \frac{\mathrm{d}n(\delta, x_s)}{\mathrm{d}\delta}\bigg|_{\delta = \frac{x_s - x_0}{D}}. \tag{A.3}$$

Using the fact that

$$\frac{\mathrm{d}n(\delta, x_s)}{\mathrm{d}x_s} = \rho_p(\delta) 2\pi \frac{x_s - x_0 - D\delta}{\beta} \rho_\mathrm{T}\left(\delta, A_{max}\right), \tag{A.4}$$

for $\delta \leq \frac{x_s - x_0}{D}$, and

$$\frac{\mathrm{d}n(\delta, x_s)}{\mathrm{d}x_s} = 0, \tag{A.5}$$

for $\delta > \frac{x_s - x_0}{D}$, and also

$$\frac{\mathrm{d}n(\delta, x_s)}{\mathrm{d}\delta}\bigg|_{\delta = \frac{x_s - x_0}{D}} = 0, \tag{A.6}$$

yields the Eq. (10) from Section 2:

$$f_+(x_s) = \int_{-\infty}^{\frac{x_s - x_0}{D}} \mathrm{d}\delta \rho_p(\delta) 2\pi \frac{x_s - D\delta - x_0}{\beta} \times \rho_\mathrm{T}\left(\delta, \frac{x_s - D\delta - x_0}{\sqrt{\beta}}\right). \tag{A.7}$$

The situation for a scraper moving into the beam along the negative x-axis is very similar. Considerations analogous to the ones given above lead to function f_-.

Appendix B. Arbitrary beam distribution algorithm derivation

As mentioned in Section 3.2, we may begin by expressing the second moment of $(x_s - x_r)$ in terms of density functions $f_\pm(x_s)$, Eqs. (10) and (11), with the variable x_r being an estimate for the central orbit coordinate x_0. We may develop the cases for the scraper blades coming from the positive and negative x_s-axis simultaneously:

$$\langle (x_s - x_r)^2 \rangle_\pm = \int_{-\infty}^{+\infty} \mathrm{d}x_s (x_s - x_r)^2 f_\pm(x_s) = \bar{x}_\pm^2 + \sigma_\pm^2 - 2\bar{x}_\pm x_r + x_r^2, \tag{B.1}$$

where $\langle \ldots \rangle$ denotes the expectation value of the quantity in the parenthesis.

Considering $x_{s\pm} = x_0 + \delta D \pm \sqrt{\beta} A$, we may write:

$$\begin{aligned} \langle (x_s - x_r)^2 \rangle_\pm &= \langle ((x_0 - x_r) + \delta D \pm \sqrt{\beta} A)^2 \rangle_\pm \\ &= (x_0 - x_r)^2 + 2(x_0 - x_r)\langle \delta \rangle D \pm 2(x_0 - x_r)\sqrt{\beta}\langle A \rangle \\ &\quad + \langle \delta^2 \rangle D^2 \pm 2D\sqrt{\beta}\langle \delta A \rangle + \beta \langle A^2 \rangle. \end{aligned} \tag{B.2}$$

Considering the definitions $\bar{\delta} = \langle \delta \rangle$, $\bar{A} = \langle A \rangle$, $\sigma_\delta^2 = \langle (\delta - \bar{\delta})^2 \rangle$, the statistical definition of the geometric transverse emittance, Eq. (1), and the usual normalisation of phase space density, Eq. (7), we can rewrite Eq. (B.2):

$$\begin{aligned} \langle (x_s - x_r)^2 \rangle_\pm &= (x_0 - x_r)^2 + D^2(\bar{\delta}^2 + {\sigma_\delta}^2) + 2\beta\epsilon_{rms} + 2(x_0 - x_r)D\bar{\delta} \\ &\quad \pm 2(x_0 - x_r)\sqrt{\beta}\bar{A} \pm 2D\sqrt{\beta}\langle \delta A \rangle. \end{aligned} \tag{B.3}$$

The above expressions allow us to put $\langle (x_s - x_r)^2 \rangle_\pm$ in terms of the rms transverse emittance ϵ_rms and the dispersive contribution $D\sigma_\delta$. However, there are additional terms $\langle A \rangle$ and $\langle A\delta \rangle$, which makes the evaluation difficult even for a known closed orbit centre x_0. In order to solve this problem, we can perform a combination of measurements from both the positive and negative x_s-axis.

Summing terms for positive and negative scraper scans in Eqs. (B.1) and (B.3) we may write:

$$\begin{aligned} &\langle (x_s - x_r)^2 \rangle_+ \\ &+ \langle (x_s - x_r)^2 \rangle_- = 2(x_0 - x_r)^2 + 2D^2(\bar{\delta}^2 + {\sigma_\delta}^2) + 4\beta\epsilon_{rms} + 4(x_0 - x_r)D\bar{\delta} \\ &\qquad = \bar{x}_+^2 + \bar{x}_-^2 + {\sigma_+}^2 + {\sigma_-}^2 - 2x_r(\bar{x}_+ + \bar{x}_-) + 2x_r^2. \end{aligned} \tag{B.4}$$

After further transformation:

$$\begin{aligned} &2\ (x_0 + D\bar{\delta} - x_r)^2 + 2D^2\sigma_\delta^2 + 4\beta\epsilon_{rms} = \\ &2\ (\frac{\bar{x}_+ + \bar{x}_-}{2} - x_r)^2 + \frac{1}{2}(\bar{x}_+ - \bar{x}_-)^2 + {\sigma_+}^2 + {\sigma_-}^2. \end{aligned} \tag{B.5}$$

Comparing coefficients in Eq. (B.5) we obtain:

$$\epsilon_{rms} = \frac{1}{4\beta}\left[\sigma_+^2 + \sigma_-^2 + \frac{(\bar{x}_+ - \bar{x}_-)^2}{2}\right] - \frac{D^2\sigma_\delta^2}{2\beta}.$$

Appendix C. Spline testing

To optimise the code for a balance between efficiency and accuracy, tests on the differentiation and integration methods were performed. Two methods were tested, one using MATLAB's piecewise polymorphic spline interpolant [25], and another using the simplified numerical methods described below.

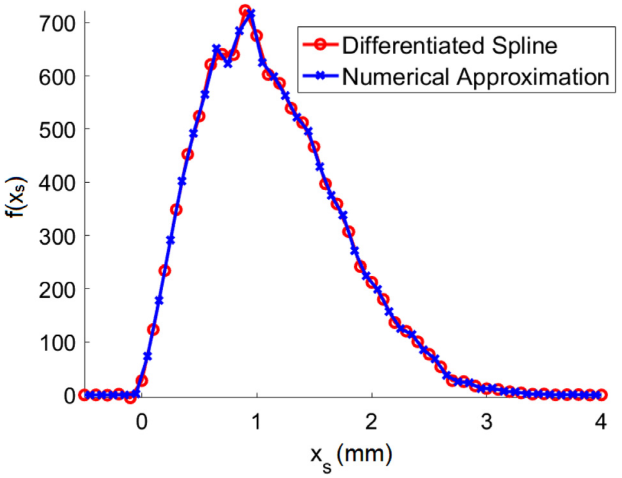

Fig. C.19. A comparison of the simple numerical vs. spline approach for a single simulation.

Begin by taking the tabulated function $F_{\pm}(x_s)$ and finding a "differentiated" value of $f_{\pm}(x_s)$ for each data entry, i:

$$f_{i,\pm} = \frac{F_{\pm,i} - F_{\pm,i+1}}{x_{\pm,i} - x_{\pm,i+1}}, \tag{C.1}$$

where $F_{\pm,i}$ is the ith entry of the beam intensity in the data set and $x_{\pm,i}$ is the corresponding scraper position.

We may combine Eq. (C.1) with the approximation

$$\int_{-\infty}^{+\infty} \mathrm{d}x_s f_{\pm}(x_s) \approx \sum_{i=1}^{n} (f_{i,\pm}(x_{\pm,i} - x_{\pm,i+1})), \tag{C.2}$$

where n is the number of entries in the data set, to obtain a simple expression for use within the algorithm:

$$\int_{-\infty}^{+\infty} \mathrm{d}x_s f_{\pm}(x_s) \approx \sum_{i=1}^{n} (F_{\pm,i} - F_{\pm,i+1}). \tag{C.3}$$

We may then calculate:

$$\sigma^2_{\delta,\pm} = \int_{-\infty}^{+\infty} \mathrm{d}x_s f_{\pm}(x_s)(x_s - \bar{x}_{\pm})^2 \approx (F_{\pm,i} - F_{\pm,i+1})(x_{\pm,i,mid} - \bar{x}_{\pm})^2, \tag{C.4}$$

where $x_{\pm,i,mid}$ is the mid point between $x_{\pm,i}$ and $x_{\pm,i+1}$ and $\bar{x}_{\pm}$ is obtained from:

$$\bar{x}_{\pm} \approx \sum_{i=1}^{n} (F_{\pm,i} - F_{\pm,i+1}) x_{\pm,i,mid}. \tag{C.5}$$

The same beam was analysed using both versions of the algorithm. For in input beam with $\epsilon_x = 1.2$ mm mrad, the two methods returned values of 1.1935 mm mrad and 1.1941 mm mrad for the spline and simplified numerical methods respectively. The difference between the results is negligible. Fig. C.19 shows a comparison of the values obtained at each point for $f_{\pm}(x_s)$ for both the spline and the simple numerical method.

We propose it would be sensible to use the more simplified method, unless the data acquisition rate is ≪400 Hz.

Appendix D. Scraper results tables

Table D.2 shows how the horizontal emittance of the beam could affect the accuracy of the algorithm. For a realistic momentum spread, a slight increase in the average error can be seen towards larger emittances, however beams with emittances much larger than 10 mm mrad would not require the level of accuracy given by the algorithm.

From Table D.3 it can be seen that the reconstruction algorithm works well up to momentum spreads much greater than are to be expected during the operation of the machine ($\sigma_\delta \approx 3 \times 10^{-4}$) for both beam distribution types. The errors on bi-Gaussian beams were consistently larger however the results remain within a satisfactory level of accuracy for the system.

Table D.2
The results from running bi-Gaussian beams with $\sigma_\delta = 3 \times 10^{-4}$ and varying horizontal emittances.

$\epsilon_{x,in}$ (mm mrad)	$\epsilon_{x,out}$ (mm mrad)	ϵ_x error (%)
0.4	0.4042	1.05
0.6	0.6060	1.01
0.8	0.8095	1.19
1.0	1.0127	1.27
1.2	1.2164	1.37
2	2.0343	1.72
4	4.0815	2.04
6	6.1385	2.31
8	8.1561	1.95
10	10.192	1.92

Table D.3
Simulation results for $\epsilon_x = 1$ mm mrad beams with varying momentum spread for Gaussian and bi-Gaussian distributions.

Gaussian		
$\sigma_\delta(\times 10^{-4})$	$\epsilon_{x,out}$ (mm mrad)	ϵ_x error (%)
1	0.9937	0.634
3	0.9945	0.546
5	0.9960	0.401
10	1.0045	0.450
Bi-Gaussian		
$\sigma_\delta(\times 10^{-4})$	$\epsilon_{x,out}$ (mm mrad)	ϵ_x error (%)
1	1.0120	1.20
3	1.0127	1.27
5	1.0143	1.43
10	1.0132	1.32

References

[1] V. Tzoganis, H.D. Zhang, A. Jeff, C.P. Welsch, Design and first operation of a supersonic gas jet based beam profile monitor, Phys. Rev. ST-AB 3 (2017) 062801.
[2] H. Burkhardt, I. Reichel, G. Roy, Transverse beam tails due to inelastic scattering, Phys. Rev. ST-AB 3 (2000) 091001.
[3] V. Lebedev, V. Shiltsev (Eds.), Accelerator Physics at the Tevatron Collider, Springer, 2014.
[4] G. Valentino, et al., Beam diffusion measurements using collimator scans in the LHC, Phys. Rev. ST-AB 16 (2013) 021003.
[5] S. Maury (Ed.), Design Study of the Antiproton Decelerator: AD, CERN/PS 96-43 (AR), 1996.
[6] V. Chohan, Beam measurement systems for the CERN Antiproton Decelerator (AD), in: Proceedings of PAC2001, Chicago, USA, 2001.
[7] V. Chohan, et al. (Ed.), Extra Low Energy Antiproton ring (ELENA) and its Transfer Lines, Design Report, CERN-2014-002, 2014.
[8] H. Schönauer, BEAMSCOPE-a novel device for measuring emittances and betatron amplitude distributions, IEEE Trans. Nucl. Sci. NS-26 (1979) 3294.
[9] T. Eriksson, private communication.
[10] S. Duarte Pinto, et al., GEM-based beam profile monitors for the antiproton decelerator, JINST 7 (2012) C03001.
[11] J. Spanggaard, GEM detectors for the transverse profile measurement of low energy antiprotons and high energy hadrons, in: Proceedings of IPAC2013, MOPWA036, Shanghai, China, 2013.
[12] W.H. Press, et al., Numerical recipies, in: The Art of Scientific Computing, third ed., Cambridge University Press, 2007, pp. 120–124 (Chapter 3).
[13] Michael Heath, Scientific Computing, McGraw-Hill, 2000, p. 324.
[14] A. Sidorin, et al., BETACOOL program for simulation of beam dynamics in storage rings, Nucl. Instrum. Methods Phys. Res. A 558 (2006) 325.
[15] A.I. Papash, et al., Nonlinear and long-term beam dynamics in low energy storage rings, Phys. Rev. ST-AB 16 (2013) 060101.
[16] J. Resta-Lopez, et al., Non-Gaussian beam dynamics in low energy antiproton storage rings, Nucl. Instrum. Methods Phys. Res. A. 834 (2016) 123.
[17] Image courtesy of Pierre Grandemange.
[18] http://mad.web.cern.ch/mad/.

[19] J. Resta-Lopez, et al., Simulation studies of the beam cooling process in presence of heating effects in the Extra Low ENergy Antiproton ring (ELENA), JINST 10 (2015) P05012.

[20] A. Piwinski, Intra-Beam Scattering, in: Proceedings of the 9th International Conference on High Energy Accelerators, Stanford, CA, 1974, p. 405.

[21] J. Bjorken, S. Mtingwa, Intrabeam scattering, Part. Accel. 13 (1983) 115.

[22] M. Martini, Intrabeam Scattering in the ACOL-AA Machines, CERN-PS-AA-84-9, 1984.

[23] A. Piwinski, Intra-Beam Scattering, CERN Report 92-01, 1992, p. 226.

[24] J. Resta-Lopez, Intra-Beam Scattering Effects in ELENA, Proceedings of IPAC2015, WEAB3, Richmond, Virginia, USA, 2015.

[25] https://uk.mathworks.com/help/matlab/ref/spline.html.